SCIENCE ADVANCES | RESEARCH ARTICLE

ENGINEERING

Wireless, skin-interfaced multimodal sensing system for continuous psychophysiological monitoring—A wearable polygraph device

Sun Hong Kim[1,2,3]†, Tae Wan Park[1]†, Seunghee Cho[1]†, Tianyu Yang[1,4]†, Seonggwang Yoo[5,6], Khaytin Ilya[7,8], Jacie R. McHaney[9], Jana Jaffe[8], Anisha Kshetrapal[8], Yue Wang[1,10], Yunyun Wu[1,11,12], Jan-Kai Chang[1], Jihun Park[1], Hak-Young Ahn[1], Min-Seung Jo[1], Jacob Trueb[1], Yei Hwan Jung[3], Seyong Oh[13], Sang Min Won[14], Debra E. Weese-Mayer[7,8]*, Jae-Young Yoo[14,15]*, John A. Rogers[1,10,16,17]*

Accurate, continuous monitoring of psychophysiological states is central to understanding stress and autonomic dysfunction across diverse medical contexts. Current approaches such as polygraphy and polysomnography rely on cumbersome, wired sensors that limit real-world utility and burden patients, particularly vulnerable populations such as infants. Here, we introduce a wireless, skin-interfaced multimodal sensing system capable of simultaneously recording cardiac, respiratory, electrodermal, and thermal signals in a time-synchronized manner. Leveraging compact and soft designs, the technology enables unobtrusive monitoring across controlled, clinical, and naturalistic settings. Validation studies performed in parallel with gold standard systems demonstrate high fidelity in quantifying stress responses during polygraph interviews, cognitive load tasks, and cold pressor tests. In pediatric sleep studies, the data reliably identify arousals, hypopnea, and apnea while revealing disease-specific autonomic signatures in infants with Down syndrome. Real-world deployment during emergency simulation training shows that multimodal stress signatures correlate inversely with performance, underscoring translational value in medical education. Machine learning analyses across all studies confirm that multimodal features outperform single-signal approaches in detecting stress and clinical events with high sensitivity and specificity. Collectively, these findings establish the technology as a next-generation wearable platform that bridges engineering innovation and clinical practice, offering mechanistic insight and diagnostic potential in stress medicine, sleep medicine, and beyond.

INTRODUCTION

Accurate monitoring of psychophysiological states is essential for understanding how stress and autonomic dysfunction manifest across a wide spectrum of medical conditions. From pediatric sleep disorders that disrupt neurodevelopment to the psychological strain experienced in high-stakes clinical settings or during polygraph examinations, subtle physiological variations in cardiac, respiratory, electrodermal, and thermal activity often serve as indicators of compromised health or heightened stress responses. These signals do not change in isolation but instead are tightly interconnected through complex autonomic pathways, such that stress alters multiple parameters in a coordinated but heterogeneous manner across individuals. Capturing these multidimensional relationships requires simultaneous multimodal sensing systems.

Conventional approaches for psychophysiological monitoring, such as polygraphy and polysomnography (PSG), rely on multiple wired sensors attached to the head, chest, and extremities (*1*, *2*). This cumbersome configuration not only limits practicality for continuous or real-world use but also introduces discomfort that can itself induce secondary stress, thereby compromising measurement accuracy. This technical complexity and patient burden often preclude routine application in clinical care, particularly for vulnerable populations such as infants and children.

Recent advances in wearable bioelectronic technologies offer an opportunity to overcome these limitations. Soft, skin-interfaced devices with wireless data transmission and multimodal sensing capabilities have the potential to capture diverse physiological signals simultaneously while minimizing discomfort and preserving data fidelity during daily activities (*3*–*6*). Despite rapid progress, however, most existing devices monitor only one or two parameters or rely on electrochemical sensors that detect sweat biomarkers (*7*–*10*). These approaches often fail to resolve the complex and dynamic interplay among multiple physiological systems. Schemes that rely on sweat are further constrained by the necessary natural or stimulated activation of sweat glands as well as the delayed response times. Thus, no single platform has yet integrated cardiac, respiratory, electrodermal, and

---

[1]Querrey Simpson Institute for Bioelectronics, Northwestern University, Evanston, IL 60208, USA. [2]Department of Chemical Engineering, University of Seoul, 163 Seoulsiripdaero, Dongdaemun-gu, Seoul 02504, Republic of Korea. [3]Department of Electronic Engineering, Hanyang University, Seoul, Republic of Korea. [4]School for Engineering of Matter, Transport and Energy, Arizona State University, Tempe, AZ 85287, USA. [5]School of Glocal Leaders, Glocal Honors College, Inje University, Gimhae 50834, Republic of Korea. [6]Department of Digital Anti-aging Healthcare, Graduate School of Inje University, Gimhae 50834, Republic of Korea. [7]Division of Autonomic Medicine, Department of Paediatrics, Ann & Robert H. Lurie Children's Hospital of Chicago, Chicago, IL 60611, USA. [8]Department of Pediatrics, Northwestern University, Feinberg School of Medicine, Chicago, IL 60611, USA. [9]Roxelyn and Richard Pepper Department of Communication Sciences and Disorders, Northwestern University, Evanston, IL 60208, USA. [10]Department of Biomedical Engineering, Northwestern University, Evanston, IL 60208, USA. [11]Department of Biomaterials and Applied Oral Sciences, Dalhousie University, Halifax, NS B3H 4R2, Canada. [12]School of Biomedical Engineering, Dalhousie University, Halifax, NS B3H 4R2, Canada. [13]Division of Electrical Engineering, Hanyang University ERICA, Ansan, Republic of Korea. [14]Department of Electrical and Computer Engineering, Sungkyunkwan University, Suwon, Republic of Korea. [15]Department of Semiconductor Convergence Engineering, Sungkyunkwan University, Suwon, Republic of Korea. [16]Department of Materials Science and Engineering, Northwestern University, Evanston, IL 60208, USA. [17]Department of Neurological Surgery, Feinberg School of Medicine, Northwestern University, Chicago, IL 60611, USA.

*Corresponding author. Email: d-weese-mayer@northwestern.edu (D.E.W.-M.); jy.yoo@skku.edu (J.-Y.Y.); jrogers@northwestern.edu (J.A.R.)

†These authors contributed equally to this work.

thermal monitoring into a miniaturized, patient-friendly system validated in both laboratory and clinical environments.

Here, we present a wireless, skin-interfaced multimodal sensing system (SIMSS) designed for continuous psychophysiological monitoring. By integrating heart rate (HR), heart rate variability (HRV), cardiac sound intensity (CSI), respiratory rate (RR), respiratory rate variability (RRV), electrodermal activity (EDA), temperature, and thermal conductivity (TC) properties into a single platform, this technology enables comprehensive assessment of autonomic and stress-related physiology in real time. Experiments demonstrate the versatility of the system across both clinical and real-world environments. Clinically, the SIMSS enables continuous monitoring of physical stress during cold pressor tests and sleep-related disturbances in pediatric patients. Beyond the clinical domain, the technology supports real-time assessment of psychological stress during polygraph interviews, reproducing and extending capabilities of conventional polygraph testing apparatus, cognitive load tasks, and stress responses during medical simulation training. Machine learning–based analysis of these multimodal data allows accurate classification of stress-related events and clinically meaningful physiological states. Collectively, these findings establish the utility of this device platform across a broad range of scenarios. The following sections present detailed descriptions of the engineering aspects, approaches to quantifying the measurements, and examples of validation against clinical and commercial standards.

RESULTS

Design concepts and device features

The devices record multiple physiological signals in a time-synchronized manner for interpretation using machine learning algorithms to associate with psychophysiological states. Figure 1A portrays a range of applications across both clinical and real-world settings, where the device mounts on the center of the chest to capture cardiac, respiratory, EDA and thermal physiological responses simultaneously. These examples include controlled scenarios for physical stress (cold pressor test) and psychological (speech-in-noise task) induction, clinical demonstrations in sleep studies, and real-world demonstrations during emergency medical training sessions. The compact size (52 mm by 48 mm by 8.5 mm), lightweight construction (7.8 g), and soft material designs enable measurements from a wide spectrum of subjects, ranging from adults to infants, without discomfort or disruption to standard medical care procedures or natural body movements, representing features that are difficult to achieve in conventional medical devices (Fig. 1B and fig. S1). Consistent signal quality can be achieved as long as the device is mounted near the center of the chest, with low sensitivity to small variations in placement location. Real-time data streams pass to a separate device with a graphical user interface for visualization. Figure 1C depicts an exploded schematic illustration that shows an inertial measurement unit (IMU; BMI160, BOSCH), a microphone (V2S; V2S200D, Knowles), an EDA sensor (MAX30009, Analog Devices), and a combined skin temperature (ST) and TC sensor. The platform also incorporates a Bluetooth low-energy (BLE) system on a chip (SoC; ISP-1807, Insight SIP), a 4-GB flash memory (MT29F4G01ABAFDWB-IT:F, Micron), and a wireless-charging coil, all mounted on a flexible printed circuit board and encapsulated in a soft silicone enclosure (figs. S2 to S4). In addition, the device exhibits low power consumption, drawing only 0.063 mA in standby mode and 3.49 mA in active mode at 3.7 V, which supports continuous monitoring for up to 37 hours. Furthermore, the system features a wireless charging scheme that enables fully recharging a depleted battery in ~6.5 hours (fig. S5).

Concurrent measurements of multiple physiological parameters associated with cardiorespiratory activity, sweat gland activity, and thermal responses of the skin are possible (Fig. 1D). The IMU and microphone enable wide-bandwidth detection of acousto-mechanic signals, including cardiac sounds (20 to 150 Hz), respiratory activity (0.1 to 1 Hz), and body orientation (~0.1 Hz) with limited disruption from ambient sounds (*11*). Extraction of parameters related to cardiac activity, including HR, HRV in the frequency domain, and CSI, relies on the Shannon energy algorithm to identify S_1 and S_2 peaks associated with cardiac sounds (*12*). CSI, derived from the acoustic intensity of cardiac valvular events, can serve as an approximate surrogate of blood pressure, with information content that complements HR and HRV in reflecting cardiovascular dynamics (*13*). This approach also allows for accurate assessment of HR, HRV, and CSI, in a manner that minimizes interference from motion artifacts (figs. S6 and S7). Monitoring of HR and CSI occurs continuously every second by averaging the intervals and sound intensities of the 10 most recent cardiac sound peaks. Similarly, HRV relies on calculations of the ratio of low-frequency (0.04 to 0.15 Hz) to high-frequency (0.15 to 0.4 Hz) power densities from these cardiac data (*14*).

Analysis of respiratory activity follows from detection of peaks in bandpass-filtered (0.1 to 1 Hz) IMU data, corresponding to chest wall movements during inhalation and exhalation. Determination of the RR results from averaging the intervals of the five most recent respiratory peaks. RRV corresponds to deviations of these intervals. These parameters of respiratory activity occur on timescales slower than those related to cardiac activity. Interpolation of RR and RRV values on 1-s intervals facilitates continuous monitoring of signals aligned to the timescale of cardiac activity. The EDA sensor measures the engagement of sweat glands, as a widely understood response to emotional or physical stress (*15*, *16*). Processing involves calculating averages and electrodermal activity standard deviations (EDA-STD) over 1-s intervals. The TC sensor measures changes in ST and TC of the skin, both influenced by near-surface blood flow. The sensor integrates a mild Joule heating element and an adjacent pair of temperature sensors to evaluate temperature and thermal transport properties at a characteristic skin depth of ~1.2 mm. Variations in these properties reflect stress-related processes such as vasoconstriction and vasodilation of capillary beds (*17*, *18*). Measurements of ST and TC occur every second and every 1.5 min, the latter necessary to capture dynamic thermal transport characteristics during heating and cooling cycles associated with activation and deactivation of the Joule heating element. TC primarily reflects sustained changes including vasomotor responses, energy metabolism, and heat generation/regulation in skin rather than rapid, second-scale acute stress responses.

Figure 1E shows representative signals, including cardiorespiratory activity, skin conductance, thermal properties of the skin, and their respective changes in response to stress. A *k*-nearest neighbors (KNN) machine learning algorithm incorporates all of these parameters to provide real-time insights into stress induced by daily and clinical activities (Fig. 1F).

Monitoring complex psychological stress induced during polygraph interviews

The first demonstrations examine the performance of the device as a wireless, wearable polygraph system. As traditionally used, polygraphy assesses psychological stresses such as those associated with anxiety,

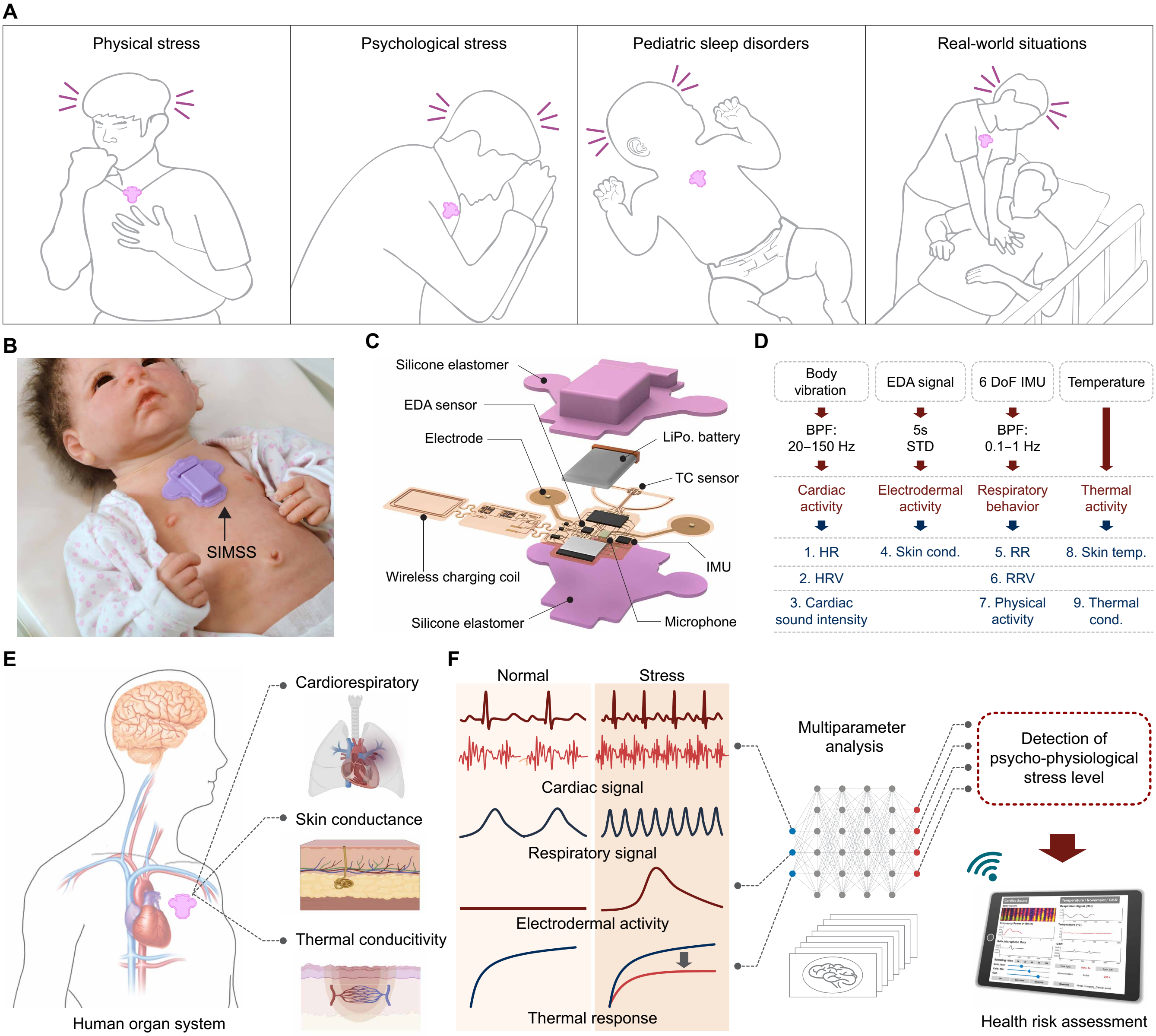

Fig. 1. Wireless, skin-interfaced multimodal system for continuous psychophysiological monitoring. (**A**) Schematic illustrations of the device used for tracking physiological signals during various forms of stress. (**B**) Photograph of a device on an infant model. (**C**) An exploded view illustration showing an IMU, a microphone, an EDA sensor, and a combined temperature and TC sensor. (**D**) Block diagram of the physiological monitoring scheme for simultaneous tracking of multiple parameters. (**E**) Illustration of SIMSS mounted on the chest for multimodal physiological monitoring. Created in BioRender. Rogers, J. (2026) https://BioRender.com/gkll5r6. (**F**) Multiparameter analysis of physiological signals for identification and quantification of psycho-physiological stress. LiPo, lithium polymer; DoF, degree of freedom; BPF, band-pass filter; SIMSS, skin-interfaced multimodal system.

fear, or nervousness, by recording multiple physiological signals in response to questioning on sensitive topics (*19*). The studies reported here rely on standardized polygraph protocols consisting of a randomized sequence of neutral control questions and emotionally sensitive questions designed to induce discomfort (Fig. 2A and fig. S8) with a device on the chest to capture multimodal signals described previously. A commercial polygraph system simultaneously records reference data from a cardiosphygmograph, pneumograph, and galvanograph placed on the arm and thorax (Fig. 2, B and C, and fig. S9). Under this configuration, comparisons examine HR, RRV, and EDA measured by the two systems to assess the physiological equivalence of SIMSS relative to the commercial polygraph (fig. S10). Strong agreement occurs across modalities, indicating that SIMSS reliably captures physiological responses comparable to those of the commercial system while providing additional multimodal sensing capabilities. Although EDA shows modestly lower correspondence due to differences in measurement location between the fingertips and the chest, both systems exhibit similar stress-related temporal patterns, confirming physiologically meaningful sympathetic activation captured by SIMSS.

Representative multimodal recordings show clear stress-evoked changes that align with responses measured by the commercial system (Fig. 2, D and E, and fig. S11). Specifically, sensitive questions

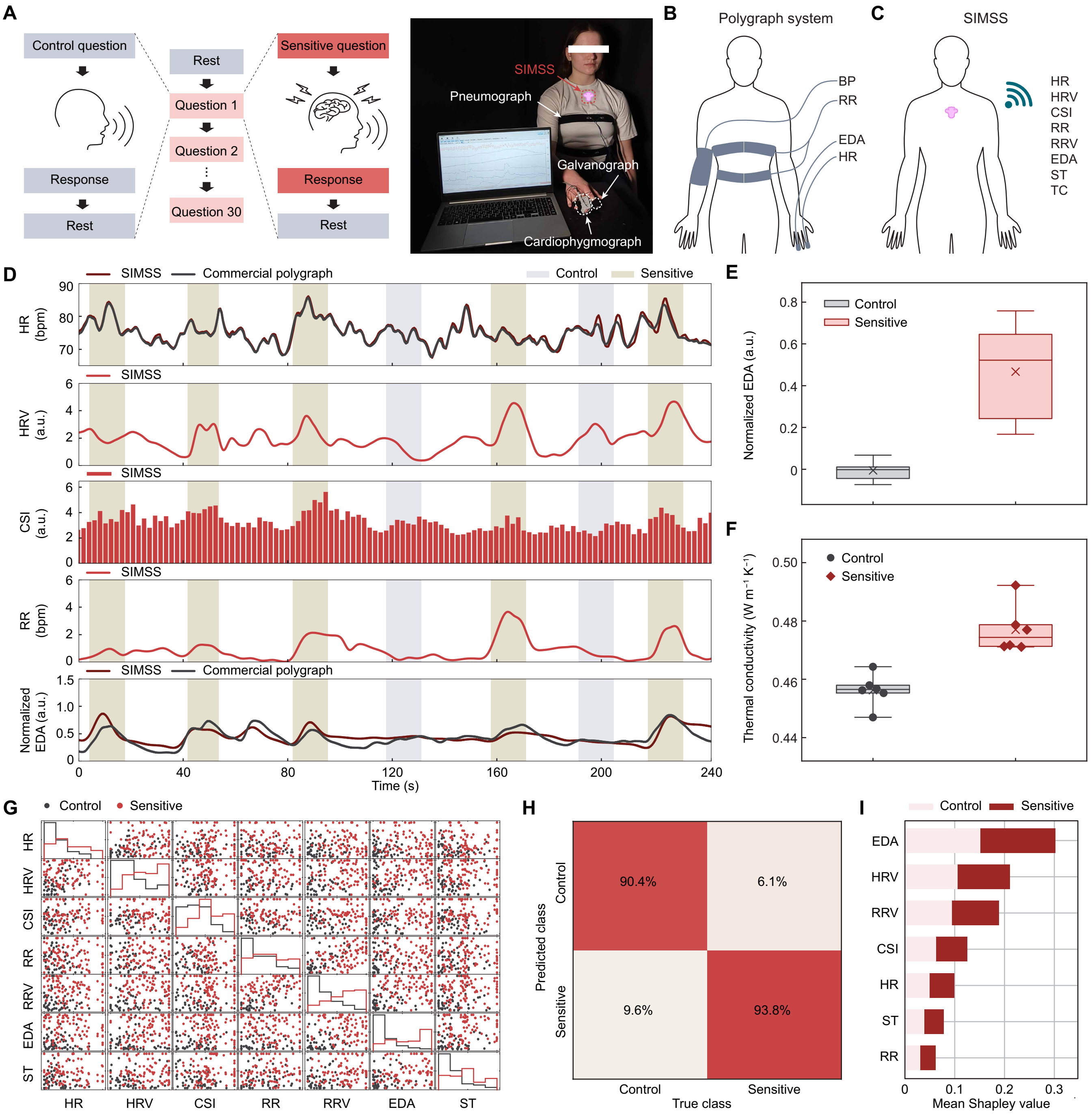

Fig. 2. Wireless, wearable monitoring of physiological parameters during polygraph interview and comparisons to a commercial polygraph system. (**A**) Protocol and experimental configuration for the polygraph interviews. (**B** and **C**) Comparison between a wired multicomponent commercial polygraph system (B) with the wireless miniaturized SIMSS (C). (**D**) Comparison of HR, HRV, CSI, RRV, and EDA data obtained with a device on the chest (red) with those measured using a commercial polygraph system (black) during interviews. Shaded areas indicate time points of responding to a question. (**E**) Box plot of normalized EDA for control (black) and sensitive (red) questions. Data are first and third quartiles (box hinges), mean (X), median (horizontal line), and lowest and highest values within 1.5 times the interquartile range (whiskers) ($n = 6$ and 360 data points). (**F**) Skin TC for control (black) and sensitive (red) questions. Data are first and third quartiles (box hinges), mean (X), median (horizontal line), minimum-maximum values (whiskers), and individual data points ($n = 6$). (**G**) A matrix of pairwise correlations among individual parameters (HR, HRV, CSI, RR, RRV, EDA, and ST) extracted from SIMSS for control (black) and sensitive (red) questions ($n = 6$ and 146 data points). (**H**) Confusion matrix displaying a model prediction for classifying control and sensitive questions. (**I**) Shapley decision plot visualizing the contribution of each physiological parameter, ranked by importance, to the model prediction shown in (G). a.u., arbitrary units.

trigger rapid increases in HRV, RRV, and EDA relative to baseline, reflecting sympathetic nervous system activation. Across six participants, group-level analysis shows average increases of 31% in EDA (SD = 11%), 21% in HRV (SD of participant means = 6%), and 16% in RRV (SD = 7%) following sensitive questions compared with controls. In addition, TC, which reflects stress-induced vasomotor responses in the cutaneous microvasculature, increases by ~10% during sensitive questioning (Fig. 2F). These results indicate that the device can detect transient stress responses across multiple physiological domains with high sensitivity.

The multimodal nature of the data enables examination of interrelationships among physiological responses during stress. Correlation analysis across HR, HRV, CSI, RR, RRV, EDA, and ST reveals coordinated but heterogeneous shifts among individuals during sensitive questioning (Fig. 2G). This heterogeneity likely stems from individual differences in autonomic reactivity, a well-established determinant of psychological stress vulnerability. A KNN classifier trained on derived features achieves 94% sensitivity and 90% specificity for classifying sensitive versus control questions. Shapley additive explanation (SHAP) analysis identifies EDA, HRV, and RRV as the strongest contributors to classification accuracy (Fig. 2, H and I), consistent with their established roles as key markers of sympathetic arousal, autonomic regulation, and respiratory control during psychological stress. Together, these features capture both rapid peripheral sympathetic activation and more gradual central adjustments in autonomic-respiratory coupling, providing a physiologically coherent explanation for their contribution to stress classification (*20*, *21*). These findings validate the device as a wireless, multimodal platform capable of reproducing the diagnostic information provided by conventional polygraphy while eliminating the need for multiple wired sensors. By enabling unobtrusive, real-time monitoring of stress-related physiological responses, this technology creates opportunities to study complex psychological stress in naturalistic settings that are inaccessible to traditional polygraph systems.

Monitoring of psychological stress

Psychological stress frequently emerges from cognitive load and anxiety during tasks that demand focused attention, such as language processing in noisy environments. Assessments of the ability of the device to capture such forms of stress involve validation studies using speech-in-noise tasks, with pupillometry as a reference standard for locus coeruleus–norepinephrine system activation (*22*). The studies include six participants who each complete 18 trials consisting of three phases: sentence presentation under varying background noise ("play sound"), verbal repetition of the sentence ("response"), and rest between trials (Fig. 3A) (*23*).

As expected, pupillometry reveals consistent pupil dilation during both listening and response phases (Fig. 3, B to D, and figs. S12 and S13), thereby validating stress induction via this multisensory challenge. Data from the device show coordinated physiological changes during both the listening and response phases of the task. HR and HRV exhibit clear elevations, accompanied by increases in CSI, RRV, and EDA, consistent with broad activation of autonomic pathways (figs. S14 to S17). These responses are most pronounced and sustained during the repetition phase. This pattern aligns with established physiology, where tasks that involve verbal responses combine cognitive load with social performance anxiety, thus eliciting heightened sympathetic drive (*24*). In addition, TC values increase slightly from 0.40 to 0.42 W m^{-1} K^{-1} on average (fig. S18), reflecting subtle stress-related vasoconstriction and microvascular alterations.

Aggregate analyses across participants confirm statistically significant increases in multiple modalities during stress versus rest (Fig. 3E). On average, CSI, RRV, and EDA increase by 1.6-fold, 2.3-fold, and 2.5-fold from baseline, respectively, although interindividual variability is notable (SD = 0.4-, 0.5-, and 0.7-fold). Despite variability in response magnitude between participants, the overall trajectory of increased multimodal activity during stress is consistent across the cohort.

Machine learning analysis further underscores the discriminative value of multimodal sensing. A KNN classifier trained on seven SIMSS features (HR, HRV, CSI, RR, RRV, EDA, and ST) distinguishes stress from rest with 87% sensitivity and 86% specificity (fig. S19). SHAP-based feature attribution highlights CSI, RRV, and EDA as the most influential parameters for classification (Fig. 3, F and G). These metrics capture distinct yet complementary autonomic processes—cardiac contractility and blood pressure dynamics (CSI), respiratory control under load (RRV), and sweat gland activity linked to sympathetic outflow (EDA)—providing mechanistic insight into the multidimensional nature of psychological stress. Specifically, the simultaneous prominence of these features indicates that cognitive stress arises from coordinated autonomic responses rather than isolated physiological changes. CSI and RRV reflect centrally mediated cardiovascular and respiratory control required to maintain cognitive effort, while EDA captures concurrent sympathetic arousal through sweat gland activity at the peripheral level (*25*–*30*). These findings establish that the device accurately detects physiological correlates of cognitive stress in naturalistic, task-based settings. Integrating cardiac, respiratory, electrodermal, and thermal signals allows for multidimensional profiling of stress reactivity, a capability directly relevant for understanding of anxiety disorders, posttraumatic stress disorder, and stress-related cardiovascular risk.

Monitoring of physical stress

Evaluations of exteroceptive physical stress rely on the cold pressor test, a well-established paradigm that provokes sympathetic activation and robust cardiovascular responses (Fig. 4A) (*31*). The protocol in this case includes a 90-s acclimation period followed by three cold pressor challenges separated by recovery intervals, with a device mounted on the chest and Food and Drug Administration (FDA)–approved reference devices for EDA on the wrist and for electrocardiogram (ECG) on the chest (*32*). Measurements of salivary cortisol serve as additional independent metrics of stress (Fig. 4B) (*33*).

Data from the device detect coordinated multimodal responses during cold pressor exposure, including elevations in HR, HRV, CSI, RR, RRV, EDA, ST, and TC, consistent with sympathetic nervous system activation (Fig. 4, C to E). Cardiac activity parameters, including HR and HRV, show close agreement with those obtained from ECG data (figs. S20 and S21). HRV exhibits excellent concordance, with an average low frequency/high frequency (LF/HF) ratio difference of only 0.002 ± 0.028 (Fig. 4D). CSI, reflecting valvular hemodynamic forces, follows trends in systolic blood pressure as measured by a continuous noninvasive monitor, thereby supporting its potential as a surrogate marker for this parameter (fig. S22) (*34*). Thermal indices also increase, with ST and TC rising in parallel with stress-induced microvascular changes (Fig. 4E and fig. S23).

Across six participants, analysis of SIMSS metrics computed at 5-s intervals reliably distinguishes stress from rest (Fig. 4F). A KNN

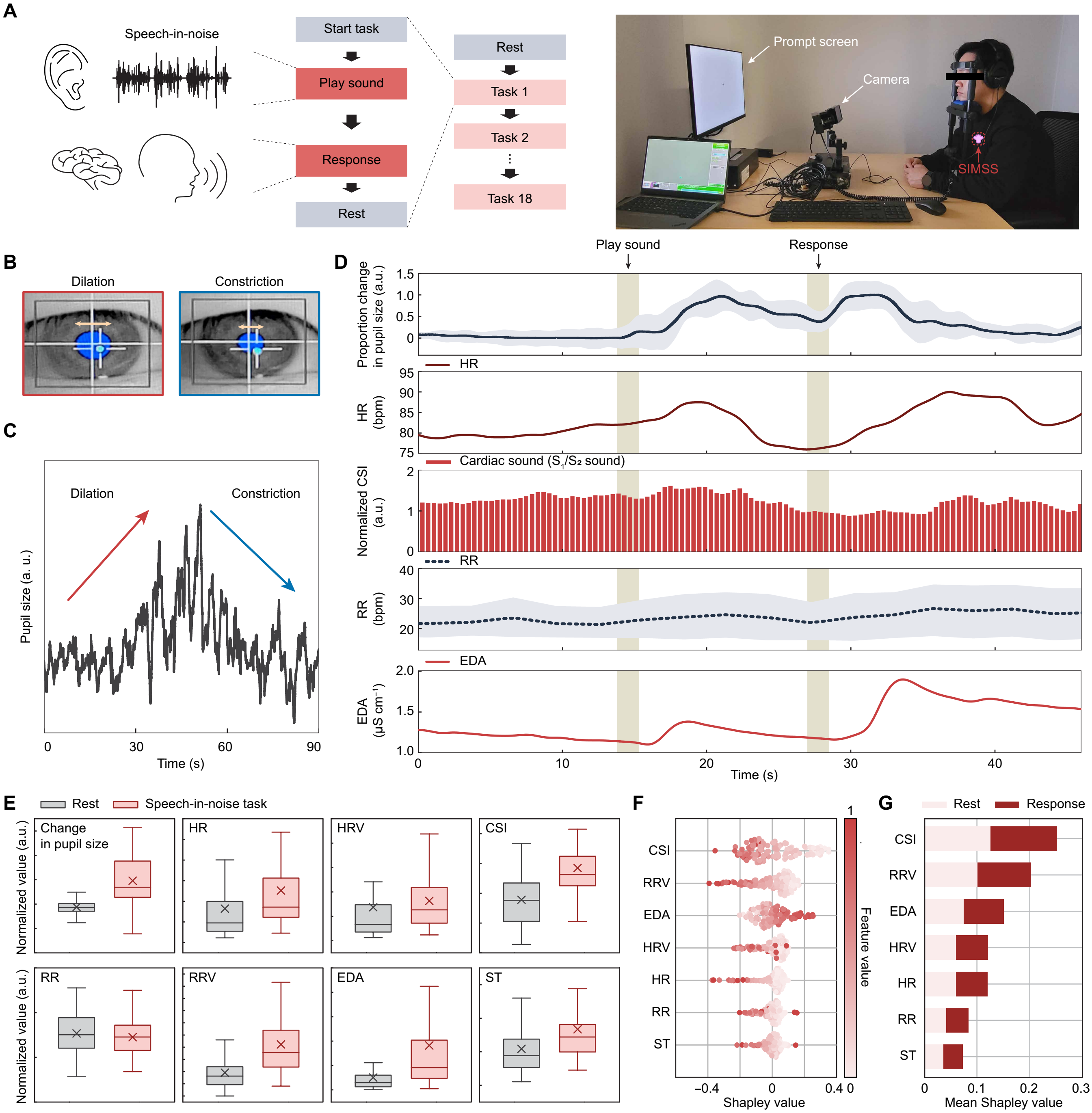

Fig. 3. Wireless, wearable monitoring of physiological parameters for detection of psychological stress. (**A**) Protocol and experimental configuration for the speech-in-noise task. (**B** and **C**) Pupillometry results including photographic recordings (B) and pupil diameter data (C). (**D**) Proportional change in pupil size during the speech-in-noise task and posttask rest (18 tasks). HR, CSI, RR, and EDA data obtained from SIMSS. Data presented as mean (line) ± SD (shaded area). (**E**) Box plots comparing physiological data (change in pupil size, HR, HRV, CSI, RR, RRV, EDA, and ST) during rest and speech-in-noise task. Data are first and third quartiles (box hinges), mean (X), median (horizontal line), and lowest and highest values within 1.5 times the interquartile range (whiskers) (*n* = 4 and 72 data points). (**F** and **G**) Shapley decision plot (F) and mean Shapley value (G) visualizing the contribution of each physiological parameter, arranged in descending order of significance, to the model prediction shown in fig. S16 (*n* = 4 and 128 data points).

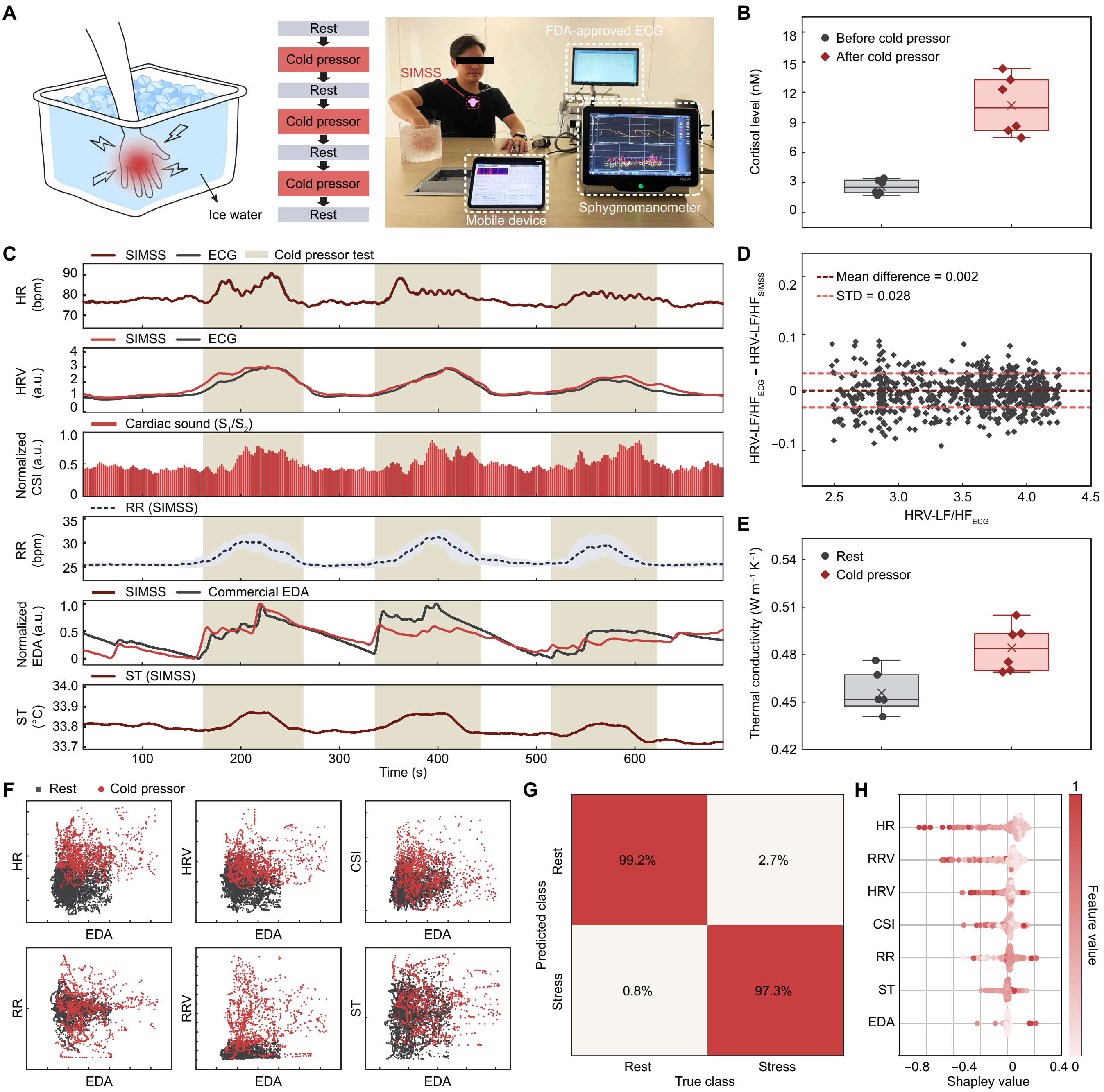
[redacted]

Fig. 4. Wireless, wearable monitoring of physiological parameters for detection of physical stress during cold pressor tests. (**A**) Protocol and experimental configuration for the cold pressor tests. (**B**) Cortisol levels before (black) and after (red) the cold pressor test ($n = 6$). (**C**) HR, HRV, CSI, RR, EDA, and ST data obtained from SIMSS (red) and those measured using standard systems (black) during cold pressor tests. Shaded areas indicate time points of the cold pressor. (**D**) Bland-Altman plot comparing HRV-LF/HF extracted from a device on the chest and a standard clinical ECG system ($n = 6$ and 735 data points). (**E**) Skin TC during rest (black) and cold pressor tests (red). Data are first and third quartiles (box hinges), mean (X), median (horizontal line), minimum-maximum values (whiskers), and individual data points ($n = 6$). (**F**) Correlations between individual parameters (HR, HRV, CSI, RR, RRV, and ST) and EDA during rest (black) and cold pressor tests (red) ($n = 6$ and 4121 data points). (**G**) Confusion matrix displaying a model prediction for classifying rest and stress ($n = 6$). (**H**) Shapley decision plot visualizing the contribution of each physiological parameter, ranked by importance, to the model prediction shown in (G) ($n = 6$ and 200 data points).

classifier trained on seven features (HR, HRV, CSI, RR, RRV, EDA, and ST) achieves 97% sensitivity and 99% specificity, substantially outperforming classifiers based on EDA alone (52% and 79%; Fig. 4G and fig. S24). SHAP analysis identifies HR and RRV as the most informative features for detecting exteroceptive stress (Fig. 4H). On average, HR increases by 10 beats per minute (bpm) with an SD of 2.6 bpm, and RRV increases by 6.5-fold with an SD of 3.1-fold across participants, highlighting both the robustness of the group-level response and the ability to capture quantifiable changes in cardiac and respiratory activity. Consistent with the SHAP analysis, HR emerges as the primary contributor, representing a rapid and robust sympathetic-driven response, while RRV serves as a secondary yet complementary feature, capturing stress-induced instability in respiratory rhythm and cardiorespiratory coupling, which helps clarify the stress-related changes of HR (*35*, *36*).

To contrast exteroceptive with interoceptive forms of stress, further experiments examine responses following COVID-19 vaccination. In this context, HRV and CSI decrease, while ST increases due to immune-mediated fever (fig. S25). Mixed stressors such as horror film viewing and roller coaster rides elicit even greater increases in HR, HRV, CSI, and EDA compared with cold pressor challenges, indicating that combined interoceptive and exteroceptive stimuli can amplify autonomic responses (figs. S26 and S27). These findings demonstrate the ability to capture robust and reproducible physiological signatures of physical stress, validating the use of the technology across controlled paradigms and highlighting its utility in distinguishing stress modalities in both clinical and real-world environments.

Monitoring of stress for pediatric sleep disorders

Sleep quality in infants is critical for neurodevelopment. Disturbances such as arousals, hypopnea, and obstructive sleep apnea represent clinically important events typically diagnosed by PSG (*37*, *38*). While PSG provides comprehensive information through electroencephalogram, ECG, pulse oximetry, and respiratory inductance plethysmography (RIP), its reliance on multiple wired sensors in a laboratory setting limits accessibility and comfort. The wireless, multimodal device introduced here offers a less obtrusive alternative for continuous overnight monitoring and characterization of these clinically relevant events.

Simultaneous recordings from pediatric patients (~7 hours) using this technology and PSG demonstrate close agreement between the two systems (Fig. 5A). During arousals, the device detects increases in HR and EDA that coincide with electroencephalogram-defined frequency shifts (Fig. 5B and figs. S28 to S30) (*39*). Hypopnea events identified by RIP occur in parallel with altered respiratory patterns from IMU signals, accompanied by electroencephalogram oscillatory changes (Fig. 5C) (*40*). Figure 5D presents continuous multimodal signals (HR, CSI, RR, EDA, and motion activity) acquired during overnight monitoring of pediatric patients, alongside PSG-based annotations of arousal, desaturation, hypopnea, and urination events. Across subjects, Bland-Altman analysis shows a mean HR difference of 0.8 ± 1.8 bpm and an HRV difference of 0.23 ± 0.2 after motion artifact suppression, demonstrating that effective removal of motion-induced artifacts enables robust and reliable cardiac monitoring despite intermittent movement during pediatric sleep (figs. S31 and S32). Motion-related artifacts accounted for only 3.4% of the total recording duration on average, indicating that physiological trajectories follow largely from continuous, directly measured signals. An additional device placed inside the diaper allows real-time detection of urination events from associated increases in electrical conductivity and temperature. Recordings from the chest reveal posturination increases in HR and CSI together with altered respiratory patterns (fig. S33). Moreover, HRV and ST demonstrate event-specific trajectories (fig. S34). Figure S35 further illustrates distinct distributions of HR, HRV, CSI, RR, and EDA across clinical states.

Machine learning analyses confirm the discriminative power of these multimodal data in this context. A KNN classifier trained on multimodal features spanning 1 min before and after annotated clinical events realizes sensitivities of 98.6% for arousal, 97.5% for hypopnea, 98.0% for desaturation, and 100% for urination, with specificities of 98.6, 96.6, 98.9, and 100%, respectively (Fig. 5E). The relative contributions of individual parameters to event classification, shown in fig. S36, reveal that respiratory patterns, cardiac activity, and ST are the dominant predictors. As in the other examples, these results highlight the essential advantages of multimodal sensing for reliable detection of stress events compared to that possible with single-modality approaches.

Infants with Down syndrome are disproportionately affected by sleep-disordered breathing due to both anatomical and physiological vulnerabilities (*41*, *42*). Hypotonia compromises airway patency, and the immaturity of the autonomic nervous system regulation impairs arousal mechanisms, leading to more frequent and severe apneic events. The device introduced here provides a unique opportunity to noninvasively investigate these mechanisms in naturalistic sleep environments. Comparative analysis between Down syndrome and healthy cohorts reveal distinctive autonomic signatures. The Down syndrome cohort exhibits significantly higher HRV-HF, indicating enhanced parasympathetic activity, whereas HRV-LF, CSI, EDA, and motion activity are lower (Fig. 5, F and G) (*43*).

Unlike conventional wearable sleep monitoring systems that rely primarily on electroencephalography or cardiorespiratory measurements, the multimodal capability of this device provides an integrated view of autonomic function by concurrently capturing cardiac, respiratory, and electrodermal dynamics. This comprehensive perspective allows detection of system-level alterations in autonomic balance during sleep that are inaccessible through traditional electroencephalography-based methods. Such altered autonomic profiles may underlie the increased susceptibility to sleep fragmentation, impaired ventilatory responses, and difficulties in sleep-wake transitions observed in Down syndrome, and they highlight the potential of SIMSS-derived markers for early risk stratification and personalized intervention in vulnerable pediatric populations.

Real-world monitoring of stress during simulation laboratory training for emergency medicine

Deployments during emergency medicine simulation training (Fig. 6A) illustrate applicability in highly dynamic environments. The curriculum includes five scenario-based sessions—bad news (session 1), seizure (session 2), apnea (session 3), ventricular tachycardia (session 4), and objective structured teaching exercise (session 5)—followed by two debriefings (figs. S37 and S38). Stress levels are estimated inversely from performance evaluation scores assigned by clinical instructors, as a behavioral benchmark.

Physiological trajectories recorded from individual participants reveal session-specific stress responses (Fig. 6B). Session 5, which emphasizes communication and teaching under pressure, shows the largest increases in HR, HRV, and CSI, consistent with the cognitive and interpersonal demands of this task. In contrast, session 2 elicits

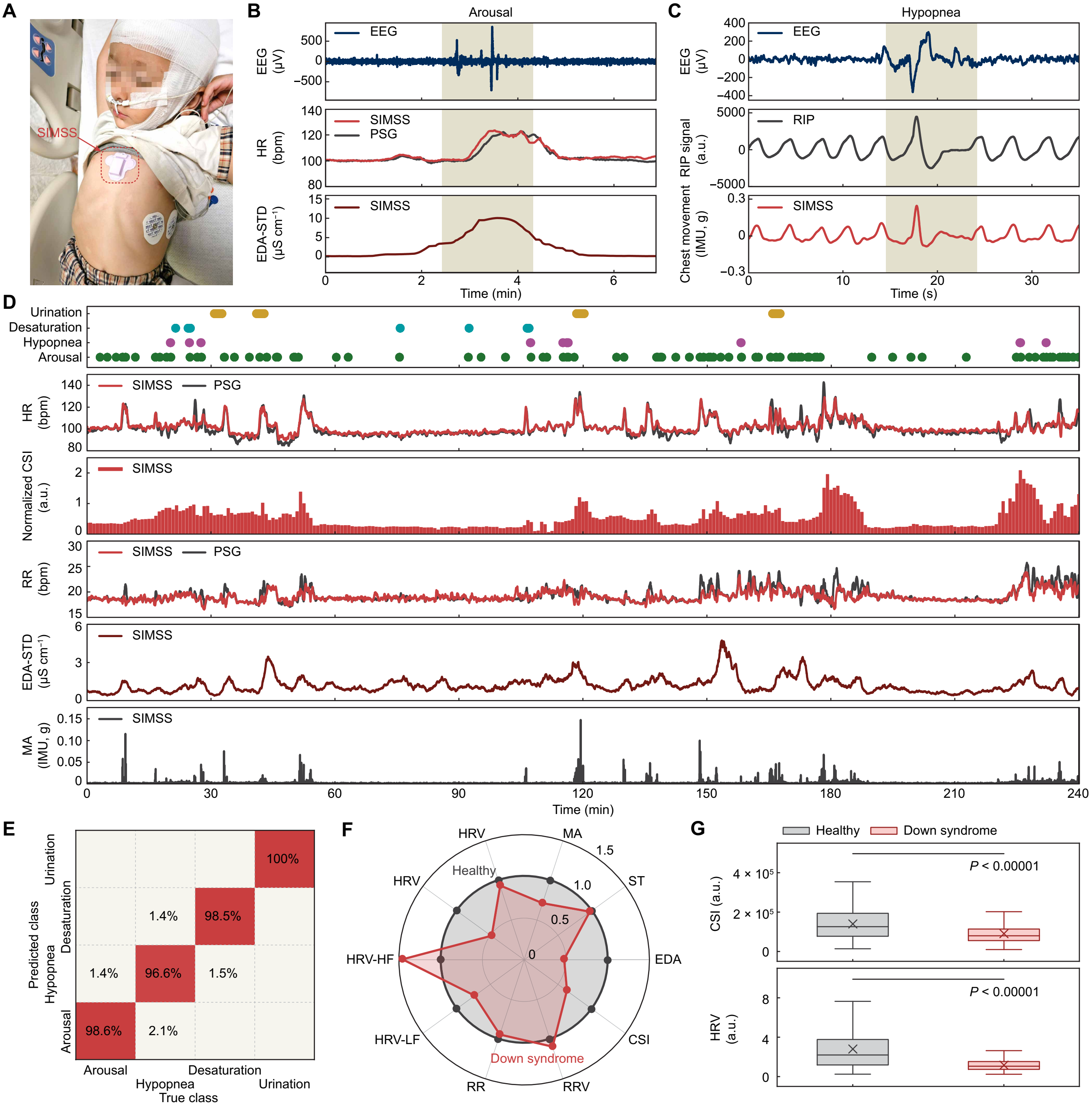

Fig. 5. Continuous, wireless monitoring of physiological parameters from pediatric patients in sleep studies. (**A**) Photograph of the SIMSS and PSG systems applied to a pediatric patient in a sleep laboratory. (**B**) Electroencephalogram (EEG) data from the PSG system, HR from SIMSS and PSG system, and EDA data from SIMSS during arousal. (**C**) EEG and RIP data from the PSG system and chest movement data during hypopnea. (**D**) HR, CSI, RR, EDA, and motion activity (MA) data recorded from a device on the chest and the PSG system during sleep with a timeline of clinical events. (**E**) Confusion matrix displaying a model prediction for classifying clinical events during sleep ($n = 13$ and 367 clinical events). (**F**) Radar chart displaying multivariate analysis comparing healthy and Down syndrome groups ($n = 13$ and 2113 data points). (**G**) Box plots comparing CSI and HRV between healthy and Down syndrome groups. Data are first and third quartiles (box hinges), mean (X), median (horizontal line), and lowest and highest values within 1.5 times the interquartile range (whiskers) ($n = 13$ and 2113 data points). One-way analysis of variance (ANOVA) was used to calculate P values.

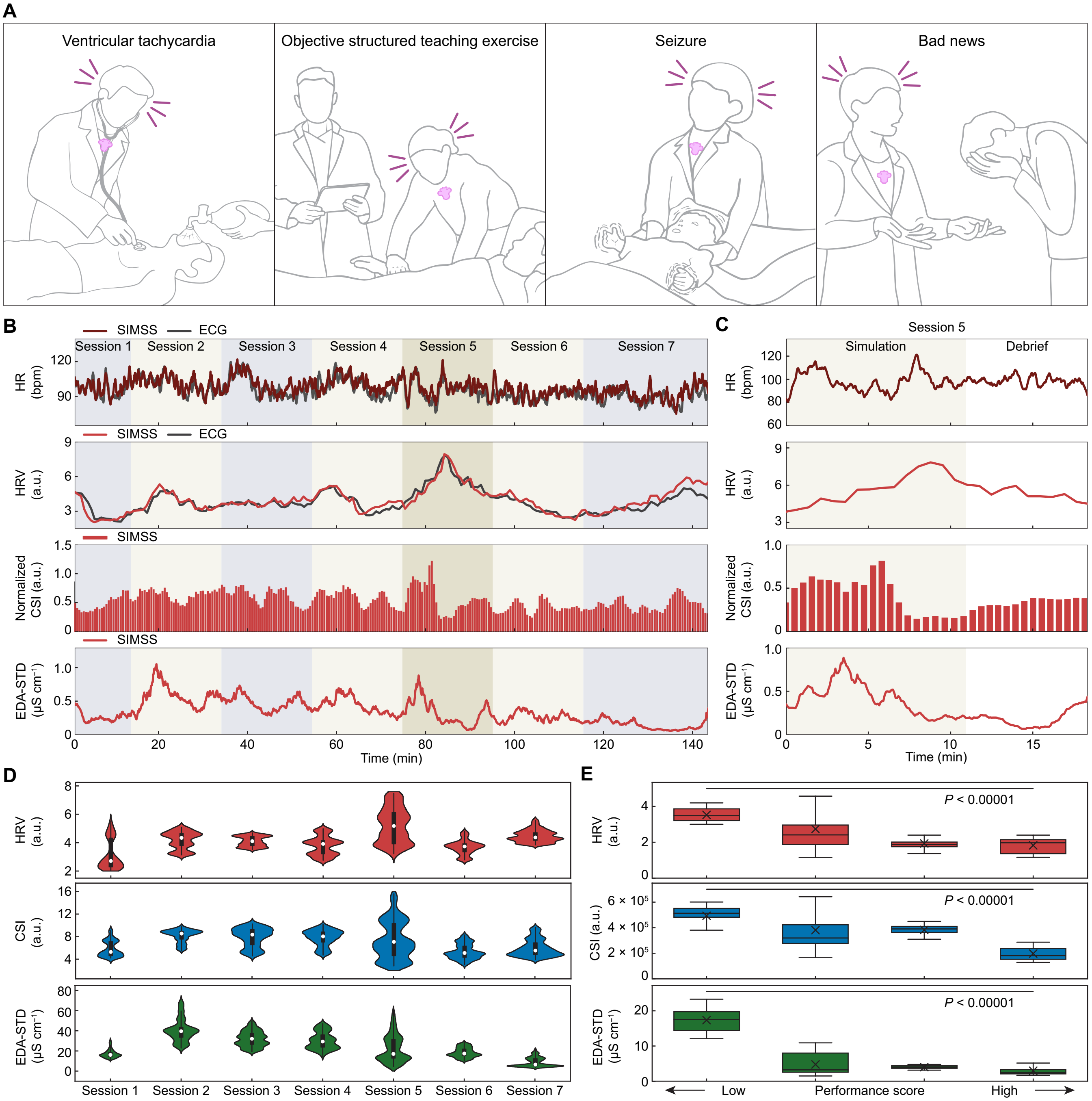

Fig. 6. Wireless, wearable monitoring of complex forms of stress during medical simulation laboratory training. (**A**) Schematic illustrations of the scenarios presented during the simulation laboratory training. (**B**) HR, HRV, CSI, and EDA data obtained from SIMSS (red) and ECG (black) during the simulation laboratory training. (**C**) Changes in HR, HRV, CSI, and EDA signals during the simulation and debrief periods of session 5. (**D**) Statistical analysis of HRV, CSI, and EDA across sessions ($n = 17$). (**E**) Box plots comparing HRV, CSI, and EDA across performance scores. Data are first and third quartiles (box hinges), mean (X), median (horizontal line), and lowest and highest values within 1.5 times the interquartile range (whiskers) ($n = 17$ and 10,382, 10,324, and 10,331 data points for HRV, CSI, and EDA, respectively). ANOVA was used to calculate P values.

the strongest EDA elevations, reflecting acute emotional stress linked to seizure management. These responses persist independently of motion artifacts, confirming that EDA changes are reliable indicators of sympathetic activation (fig. S39). Quantitative analysis further confirms the reliability of cardiac monitoring during simulation tasks characterized by abrupt and high-amplitude movements. Bland-Altman comparison with reference ECG measurements shows mean differences of 2.2 ± 2.1 bpm for HR and 0.6 ± 0.4 for HRV after motion artifact suppression (fig. S40). Moreover, motion-related artifacts account for only a small fraction of the total recording duration, averaging 4.2% across sessions, supporting the conclusion that the observed physiological patterns predominantly arise from continuously acquired signals rather than interpolated segments. Within single sessions, stress responses shift markedly between active simulation and debriefing phases. For example, HR, HRV, CSI, and EDA all increase substantially during scenario execution but decrease toward baseline during debriefing (Fig. 6C).

At the group level, distinct patterns emerge across sessions (Fig. 6D). HRV and CSI display the greatest variability in session 5, highlighting their sensitivity to complex, multifactorial stressors, whereas EDA shows pronounced but less consistent changes across sessions 2, 4, and 5. On average, HRV, CSI, and EDA increase by 130, 260, and 360% relative to baseline in session 5, with wide interindividual variability, reflecting heterogeneous stress reactivity among participants.

Crucially, physiological changes in session 5 demonstrate an inverse relationship with performance scores (Fig. 6E). Residents who exhibit greater increases in HRV, CSI, and EDA during the scenario tend to achieve lower evaluations, suggesting that heightened physiological stress may impair clinical performance. These results establish the devices introduced here as multimodal tools for quantifying stress responses in realistic training environments and underscore their potential role in guiding educational strategies aimed at improving resilience and task performance in high-stakes medical practice.

DISCUSSION

This work presents a wireless, multimodal sensing system that integrates cardiac, respiratory, electrodermal, and thermal measurements into a compact, skin-interfaced form for real-time psychophysiological monitoring. By consolidating multiple physiological domains traditionally captured through separate wired systems, this technology enables comprehensive assessment of autonomic and stress-related processes in both controlled and dynamic environments. Demonstrations across polygraph testing, cognitive stress tasks, cold pressor challenges, pediatric sleep studies, and medical simulation training establish the fidelity, versatility, and clinical relevance of the device.

A particularly notable contribution lies in pediatric sleep medicine. Simultaneous comparison with PSG confirms the ability to detect arousals, hypopnea, and apnea while also providing mechanistic insights into autonomic regulation. In infants with Down syndrome, multimodal analysis reveals attenuated sympathetic responsiveness and parasympathetic dominance, consistent with known vulnerabilities in airway patency and autonomic control. Such disease-specific autonomic signatures may serve as valuable biomarkers for risk stratification, early diagnosis, and targeted intervention in neurodevelopmental disorders.

Beyond pediatric populations, the technology demonstrates robust performance in practical environments such as emergency medicine simulation. Multimodal stress signatures captured during training correlate inversely with clinical performance, underscoring the potential utility for educational assessment, resilience training, and performance optimization. This ability to link physiological stress reactivity with functional outcomes represents an important advance over conventional stress monitoring methods.

The multimodal approach also proves critical for disambiguating stress states. While single modalities such as EDA can capture sympathetic activation, they are susceptible to artifacts and lack specificity. By integrating acousto-mechanical cardiac signals, respiratory variability, and thermal dynamics, the present technology enables machine learning models to achieve superior classification performance and mechanistic interpretability. The identification of condition-specific feature importance—for example, HRV and CSI in cognitive stress versus HR and RRV in physical stress—demonstrates its potential for personalized profiling of stress physiology.

These advantages stem from fundamental differences in sensing architecture and measurement capability compared with existing wearable systems (table S1). Unlike conventional devices that rely on one or two physiological channels, the present platform uniquely combines cardiac, respiratory, electrodermal, and thermal sensing within a single compact form factor, enhancing both specificity and robustness in real-world environments. Moreover, the results follow from the use of entirely dry, nonchemical modalities—avoiding the limitations of sweat-dependent chemical sensors that face challenges in cleaning, reuse, and long-term stability.

Beyond these demonstrated applications, the system's capability for continuous autonomic monitoring holds promise in several emerging clinical domains. In intensive care settings, real-time multimodal sensing could complement traditional vital sign monitoring to provide early warnings of autonomic instability or sepsis-related stress. In mental health therapy, longitudinal tracking of sympathetic-parasympathetic balance may assist in quantifying treatment response and emotional regulation in conditions such as posttraumatic stress disorder. Similarly, in disorders of gut-brain interaction—including irritable bowel syndrome and functional dyspepsia—continuous assessment of autonomic tone may help elucidate the physiological coupling between visceral stress and neural regulation.

In summary, this technology represents a clinically translatable, multimodal platform that captures psychophysiological stress and sleep-related events with high fidelity across laboratory, clinical, and real-world contexts. By extending its application to intensive care, behavioral health, and neurovisceral medicine, this system could further bridge physiological sensing and precision therapeutics. By uncovering mechanistic links between autonomic imbalance, stress reactivity, and health outcomes, these devices have the potential to transform diagnostic workflows, optimize educational programs, and enable personalized therapeutic monitoring across stress medicine, pediatrics, and behavioral health.

MATERIALS AND METHODS

Design and fabrication

The device consists of eight main components: an IMU (BMI160, BOSCH), a microphone (V2S200D, Knowles), an EDA sensor (MAX30009, Analog Devices), a combined temperature and TC sensor, a flash memory module (MT29F4G01ABAFDWB-IT:F, Micron), a Bluetooth SoC (ISP-1807, Insight SIP), and a hardware system for power delivery and wireless charging. The power delivery and wireless charging components are mounted on a separate island of a flexible printed circuit board that includes serpentine traces as interconnects to enable mechanical compliance. The IMU delivers three-axis acceleration data at a sampling rate of 104 Hz to the Bluetooth SoC via serial peripheral interface communication protocols. Both the microphone data, sampled at 1 kHz, and the IMU data, sampled at 104 Hz, pass into a 4-GB flash memory, capable of storing data for up to 16 hours of continuous recording. The wireless charging and power components include a charging coil with a resonance frequency of 13.56 MHz, a voltage rectifier, a voltage regulator, green light-emitting diode as charging indicator, a battery charger integrated circuit, and a 3.7-V, 110-mAh lithium-polymer battery. A commercial interface (Segger Embedded Studio) enabled upload of customized firmware to the Bluetooth SoC. A silicone elastomer (Silbione-4420) formed the encapsulation layers, designed to allow exposure of the electrodes for the EDA sensor for an electrical interface to the skin via a commercially available hydrogel adhesive (km10a, Katecho). The device mounts on the skin with a medical-grade adhesive (2477P, 3M, Medical Materials and Technologies) that is approved for use in bandages according to International Organization for Standardization 10993-5 standards, suitable for the delicate skin of preterm infants (fig. S41). Furthermore, to confirm that multimodal integration does not introduce mechanical or thermal coupling and that each sensor can be operated stably and independently within the system, we conducted controlled vibration and thermal stimulation experiments by comparing responses from the multimodal device with those from corresponding standalone sensors, demonstrating strong agreement and minimal cross-sensor interference (figs. S42 and S43).

Data analytics

Processing of data measured by the microphone used a band-pass filtering with lower and upper cutoff frequencies of 20 and 150 Hz, respectively. This filtering process effectively separated cardiac sounds from features caused by motion artifacts and vocalization. Calculations of HR used cardiac sound signals converted to Shannon energy based on Eq. 1, where S is the Shannon energy and C is the cardiac sound, to yield clear peaks associated with cardiac cycles

$$S = C \times \log(C) \tag{1}$$

The peaks of the Shannon energy envelope defined the timing of the S_1 and S_2 features, allowing for calculations of HR interval. The amplitude ratio of S_2/S_1 served as the basis for CSI. HR and CSI were continuously monitored every second by averaging the intervals and sound intensities of the 10 most recent cardiac sound peaks.

The power spectral density followed from short-term Fourier transform of the filtered signal. Summation of the power spectral density data across a low frequency (0.04 to 0.15 Hz) and a high frequency (0.15 to 0.4 Hz) range yielded HRV in the LF and HF ranges, respectively.

Calculations of RR from the IMU data used intensity peaks corresponding to inhalation events for peak-to-peak intervals. The values of RR and RRV followed from averaging the intervals between the five most recent respiratory peaks and calculating the deviations in these intervals, respectively.

Analysis of data from the EDA sensor used band-pass filtering with cutoff frequencies of 0.1 and 1 Hz. Average and SDs of EDA data over time windows of 1-s yielded values for EDA and EDA-STD, respectively. All signals were interpolated at 1-s intervals to yield common timescales for all continuous monitoring parameters.

Measurements of ST and TC used calibrations based on two skin-like poly(dimethylsiloxane) phantoms (skin phantoms) with known thermal conductivities at the upper and lower limits of those associated with human skin. Values of TC followed from comparisons of measured changes in temperature due to Joule heating at a fixed electrical power with those realized with the phantoms. The TC followed from interpolation, as verified by our previous work (*18*). A second pair of temperature sensors at a large distance (1.5 cm) from the heating element defined the baseline temperature, to allow subtraction of variations due to changes in the ambient.

Human subject studies

All individuals participated voluntarily, and informed consent was obtained before the experiments. Research protocols were approved by the Institutional Review Board at Northwestern University (STU00221965, STU00219433-MOD0004, and STU00221424) and Lurie Children's Hospital (2022-5654 and 2024-6768)

Polygraph interviews and measurements using a commercial polygraph system

Data were collected from seven subjects during polygraph interview sessions with SIMSS mounted on the center of chest and a commercial polygraph system interfaced in the standard manner (Biofeedback, BioSignals), with sensors worn on the fingers to measure EDA, photoplethysmography sensors worn on the finger to measure cardiac signals including HR and HRV, and RIP bands worn on the chest to measure respiratory signals. Table S2 summarizes the participant information in the study of polygraph interview. The subjects relaxed for 10 min to maintain resting status before the interview session, which consisted of two sets of 30 questions, with each question categorized as either control or sensitive, presented using a prompt screen to eliminate social context. The order of the questions was randomized. The interval between each question was at least 30 s to allow physiological responses to return to baseline. For data analysis, we refined the processing pipeline to improve sensitivity to rapid stress-linked responses. A 5-s moving average window was applied to preserve temporal resolution, and feature extraction was optimized by identifying the time point corresponding to the maximum derivative within each question period. Multimodal features (HR, HRV, CSI, RR, RRV, EDA, ST, and TC) were then extracted from a 5-s window centered on this point. These features were subsequently used as inputs for machine learning, enabling more accurate detection of abrupt physiological changes during questioning.

Speech-in-noise tests and pupillary assessment

Physiological signals were recorded from the chest. A commercial pupillometry system yielded measurements for comparisons. Specifically, the monocular left eye pupillary response was recorded at 1000 Hz using an Eyelink 1000 Plus Desktop Mount (SR Research) with a chin and forehead rest for stabilization. Luminance of the visual field was controlled with consistent, low-level ambient lighting across all participants. A nine-point eye tracker calibration was performed before testing. The participants completed a speech-in-noise test, a clinical standard for speech perception in noise abilities. The test consisted of three lists of six stimuli, corresponding to spoken sentences masked in four-talker background noise at signal-to-noise ratio levels of 25, 20, 15, 10, 5, and 0 dB, respectively. A 100-ms, 1000-Hz tone signaled the start of each task, followed by 2 s of silence, then the background masker. The background masker began 3 s before the target sentence and continued for 2 s after the end of the target sentence. Participants maintained gaze on a fixation cross on the screen during listening. Target sentences varied in duration from 2.3 to 3.6 s. A 2-s period of silence and a 100-ms, 1000-Hz tone followed the background masker to signal the end of the sentence. Participants then repeated the sentence to the best of their ability. The interval between each task was 30 s to allow physiological responses to return to baseline and control synchronization across devices before the start of the next task. Processing and analysis methods for pupillometry data followed previously reported approaches (*44*, *45*). The rest state corresponds to the 10-s baseline data recorded before the speech-in-noise task. Data were first down-sampled to 50 Hz and then processed to remove noise from blinks and saccades. Tasks with more than 15% of data points detected as blinks or saccades were removed. For the remaining tasks, missing data points due to blinks or saccades were linearly interpolated to 150 ms before and after the missing data points. Pupil responses were normalized to baseline on a task-by-task basis to the average 500 ms before the onset of stimulus.

Cold pressor tests

Physiological signals were recorded from the chest. A medical-grade ECG recording system and an FDA-approved EDA sensor served as standards for comparison of certain cardiac parameters and skin conductivity, respectively. The study began with subjects in a resting status with eyes closed for 3 min. The subjects then placed one hand in cold water (0° to 4°C) for 30 s or more, as a source of psychological stress. After removing their hand from the cold water, subjects rested again for 3 min. For salivary cortisol analysis, participants avoided food consumption 1 hour before measurement. Before sampling, participants rinsed their mouth with water to remove food residue and waited 10 min. Collection of saliva samples occurred first during rest (before cold pressor test) and second while under stress (after cold pressor test). Considering that salivary cortisol levels typically show a marked increase ~10 min after stress induction, saliva samples were collected 10 min after completion of the cold pressor test (*46*). A passive drooling method allowed collection of unstimulated whole saliva samples into a plastic tube. Samples were vortexed and centrifuged at 1500*g* for 15 min. A salivary cortisol assay kit (Salimetrics LLC, Philadelphia, PA, USA) yielded cortisol levels.

Pediatric sleep monitoring and PSG measurements

Thirteen pediatric patients with a median age of 20.4 months (minimum, 7 months; maximum, 30 months) were included in the sleep study (table S3). Devices were mounted on the chests of patients without interfering with the clinical PSG systems. The PSG system supported measurements of ECG, electroencephalogram, transcutaneous CO_2, digital pulse oximetry, and RIP. For the detection urination, a device equipped with temperature and EDA sensors was attached to the inside of the diaper. A device attached on chest monitored the motion activity, calculated as the square root of the sum of the squared x, y, and z components collected from the IMU for tracking the subtle chest movements at clinical events. Application of an accelerometer-based motion artifact suppression method improved the fidelity of EDA recordings (fig. S44). Motion artifacts were identified as periods where the magnitude of the acceleration exceeded 0.1 g. EDA values during these intervals were masked as missing data. Contiguous missing segments were reconstructed using linear interpolation. This procedure effectively suppressed motion-induced artifacts while preserving the underlying physiological dynamics of the EDA signals for subsequent analysis.

Simulation laboratory training

The study involved 16 second-year pediatric residents participating in the simulation laboratory training (table S4). Each participant was equipped with a device mounted on their chest and an additional wearable patch-type, FDA-approved ECG recording device to serve as a reference. Data were collected across seven session rooms, with each session lasting 18 min, followed by a 2-min transition period to the next session. Simulated sessions were designed to assess skills in medical management, communication, teamwork, and leadership. After completing all simulations, participants took part in a short debriefing session. The wearable devices were then removed following the debrief. Application of an accelerometer-based motion artifact suppression method improved the fidelity of physiological signals (fig. S44). Motion artifacts were identified as periods where the magnitude of the acceleration exceeded 0.1 g. EDA values during these intervals were masked as missing data. Contiguous missing segments were reconstructed using linear interpolation. Similar procedures were applied to cardiac data but with masking across not only the motion artifact intervals but also two beat cycles before and after these intervals to account for transient contamination. Linear interpolation yielded continuous HR and HRV trajectories. This approach follows current methodological guidelines recommending interpolation rather than simple exclusion of artifact-laden segments to preserve temporal continuity and the validity of HRV estimation (*47*). These procedures minimized the influence of motion artifacts on cardiovascular and electrodermal signals and ensured close agreement with reference ECG measurements.

Data statistics

Statistical analysis of data used one-way multivariate analysis of variance performed in MATLAB, with an assumption of normal distributions for data points for each group. Number of data points and subjects involved for each analysis can be found in the corresponding figure captions.

Supplementary Materials

This PDF file includes:

Figs. S1 to S44

Tables S1 to S4

REFERENCES

1. L. Sousedikova, M. Adamek, M. Hromada, in *2022 26th International Conference on Circuits, Systems, Communications and Computers (CSCC)* (IEEE, 2022), pp. 1–5.
2. S. R. Pandi-Perumal, D. W. Spence, A. S. BaHammam, "Polysomnography: An overview," in *Primary Care Sleep Medicine: A Practical Guide* (Springer, 2014), pp. 29–42.
3. D. Son, J. Lee, S. Qiao, R. Ghaffari, J. Kim, J. E. Lee, C. Song, S. J. Kim, D. J. Lee, S. W. Jun, S. Yang, M. Park, J. Shin, K. Do, M. Lee, K. Kang, C. S. Hwang, N. Lu, T. Hyeon, D.-H. Kim, Multifunctional wearable devices for diagnosis and therapy of movement disorders. *Nat. Nanotechnol.* **9**, 397–404 (2014).
4. S. H. Kim, A. Basir, R. Avila, J. Lim, S. W. Hong, G. Choe, J. H. Shin, J. H. Hwang, S. Y. Park, J. Joo, C. Lee, J. Choi, B. Lee, K.-S. Choi, S. Jung, T.-I. Kim, H. Yoo, Y. H. Jung, Strain-invariant stretchable radio-frequency electronics. *Nature* **629**, 1047–1054 (2024).
5. H. Jeong, J. Y. Lee, K. Lee, Y. J. Kang, J.-T. Kim, R. Avila, A. Tzavelis, J. Kim, H. Ryu, S. S. Kwak, J. U. Kim, A. Banks, H. Jang, J.-K. Chang, S. Li, C. K. Mummidisetty, Y. Park, S. Nappi, K. S. Chun, Y. J. Lee, K. Kwon, X. Ni, H. U. Chung, H. Luan, J.-H. Kim, C. Wu, S. Xu, A. Banks, A. Jayaraman, Y. Huang, J. A. Rogers, Differential cardiopulmonary monitoring system for artifact-canceled physiological tracking of athletes, workers, and COVID-19 patients. *Sci. Adv.* **7**, eabg3092 (2021).
6. H. U. Chung, A. Y. Rwei, A. Hourlier-Fargette, S. Xu, K. Lee, E. C. Dunne, Z. Xie, C. Liu, A. Carlini, D. H. Kim, D. Ryu, E. Kulikova, J. Cao, I. C. Odland, K. B. Fields, B. Hopkins, A. Banks, C. Ogle, D. Grande, J. B. Park, J. Kim, M. Irie, H. Jang, J. Lee, Y. Park, J. Kim, H. H. Jo, H. Hahm, R. Avila, Y. Xu, M. Namkoong, J. W. Kwak, E. Suen, M. A. Paulus, R. J. Kim, B. V. Parsons, K. A. Human, S. S. Kim, M. Patel, W. Reuther, H. S. Kim, S. H. Lee, J. D. Leedle, Y. Yun, S. Rigali, T. Son, I. Jung, H. Arafa, V. R. Soundararajan, A. Ollech, A. Shukla, A. Bradley, M. Schau, C. M. Rand, L. E. Marsillio, Z. L. Harris, Y. Huang, A. Hamvas, A. S. Paller, D. E. Weese-Mayer, J. Y. Lee, J. A. Rogers, Skin-interfaced biosensors for advanced wireless physiological monitoring in neonatal and pediatric intensive-care units. *Nat. Med.* **26**, 418–429 (2020).
7. S. Shin, R. Liu, Y. Yang, J. A. Lasalde-Ramírez, G. Kim, C. Won, J. Min, C. Wang, K. Fan, H. Han, C. Uwakwe, W. Heng, T. K. Hsiai, Z. Li, J. D. FitzGerald, W. Gao, A bioinspired microfluidic wearable sensor for multiday sweat sampling, transport, and metabolic analysis. *Sci. Adv.* **11**, eadw9024 (2025).

8. J. Kim, S. Oh, D. S. Yang, L. Rugge, R. Mathur, S. S. Kwak, S. Yoo, S. Li, E. E. Kanatzidis, G. Lee, H.-J. Yoon, Y. Huang, R. Ghaffari, S. A. McColley, J. A. Rogers, A skin-interfaced, miniaturized platform for triggered induction, capture and colorimetric multicomponent analysis of microliter volumes of sweat. *Biosens. Bioelectron.* **253**, 116166 (2024).
9. S. Imani, A. J. Bandodkar, A. M. V. Mohan, R. Kumar, S. Yu, J. Wang, P. P. Mercier, A wearable chemical–electrophysiological hybrid biosensing system for real-time health and fitness monitoring. *Nat. Commun.* **7**, 11650 (2016).
10. S. Cho, S. M. Shaban, R. Song, H. Zhang, D. Yang, M.-J. Kim, Y. Xiong, X. Li, K. Madsen, S. Wapnick, S. Zhang, Z. Chen, J. Kim, G. Guinto, M. Li, M. Lee, R. F. Nuxoll, S. Shajari, J. Wang, S. Son, J. Shin, A. J. Aranyosi, D. E. Wright, T.-I. Kim, R. Ghaffari, Y. Huang, D.-H. Kim, J. A. Rogers, A skin-interfaced microfluidic platform supports dynamic sweat biochemical analysis during human exercise. *Sci. Transl. Med.* **16**, eado5366 (2024).
11. J.-Y. Yoo, S. Oh, W. Shalish, W.-Y. Maeng, E. Cerier, E. Jeanne, M.-K. Chung, S. Lv, Y. Wu, S. Yoo, A. Tzavelis, J. Trueb, M. Park, H. Jeong, E. Okunzuwa, S. Smilkova, G. Kim, J. Kim, G. Chung, Y. Park, A. Banks, S. Xu, G. M. Sant'Anna, D. E. Weese-Mayer, A. Bharat, J. A. Rogers, Wireless broadband acousto-mechanical sensing system for continuous physiological monitoring. *Nat. Med.* **29**, 3137–3148 (2023).
12. M. M. Milani, P. E. Abas, L. C. De Silva, A critical review of heart sound signal segmentation algorithms. *Smart Health* **24**, 100283 (2022).
13. R.-C. Peng, W.-R. Yan, N.-L. Zhang, W.-H. Lin, X.-L. Zhou, Y.-T. Zhang, Cuffless and continuous blood pressure estimation from the heart sound signals. *Sensors* **15**, 23653–23666 (2015).
14. R. Castaldo, P. Melillo, U. Bracale, M. Caserta, M. Triassi, L. Pecchia, Acute mental stress assessment via short term HRV analysis in healthy adults: A systematic review with meta-analysis. *Biomed. Signal Process. Control* **18**, 370–377 (2015).
15. C. Xu, Y. Song, J. R. Sempionatto, S. A. Solomon, Y. Yu, H. Y. Y. Nyein, R. Y. Tay, J. Li, W. Heng, J. Min, A. Lao, T. K. Hsiai, J. A. Sumner, W. Gao, A physicochemical-sensing electronic skin for stress response monitoring. *Nat. Electron.* **7**, 168–179 (2024).
16. H. Kim, Y.-S. Kim, M. Mahmood, S. Kwon, N. Zavanelli, H. S. Kim, Y. S. Rim, F. Epps, W.-H. Yeo, Fully integrated, stretchable, wireless skin-conformal bioelectronics for continuous stress monitoring in daily life. *Adv. Sci.* **7**, 2000810 (2020).
17. R. C. Webb, Y. Ma, S. Krishnan, Y. Li, S. Yoon, X. Guo, X. Feng, Y. Shi, M. Seidel, N. H. Cho, J. Kurniawan, J. Ahad, N. Sheth, J. Kim, J. G. Taylor VI, T. Darlington, K. Chang, W. Huang, J. Ayers, A. Gruebele, R. M. Pielak, M. J. Slepian, Y. Huang, A. M. Gorbach, J. A. Rogers, Epidermal devices for noninvasive, precise, and continuous mapping of macrovascular and microvascular blood flow. *Sci. Adv.* **1**, e1500701 (2015).
18. S. R. Madhvapathy, Y. Ma, M. Patel, S. Krishnan, C. Wei, Y. Li, S. Xu, X. Feng, Y. Huang, J. A. Rogers, Epidermal electronic systems for measuring the thermal properties of human skin at depths of up to several millimeters. *Adv. Funct. Mater.* **28**, 1802083 (2018).
19. J. Synnott, D. Dietzel, M. Ioannou, A review of the polygraph: History, methodology and current status. *Crime Psychology Review* **1**, 59–83 (2015).
20. R. Lima, D. F. de Noronha Osório, H. Gamboa, "Heart rate variability and electrodermal activity in mental stress aloud: Predicting the outcome," in *Proc. 12th Int. Joint Conf. Biomed. Eng. Syst. Technol.* (SciTePress, 2019), pp. 42–51.
21. A. Boffet, L. M. Arsac, V. Ibanez, F. Sauvet, V. Deschodt-Arsac, Detection of cognitive load modulation by EDA and HRV. *Sensors* **25**(8), 2343 (2025).
22. G. Aston-Jones, J. D. Cohen, An integrative theory of locus coeruleus-norepinephrine function: Adaptive gain and optimal performance. *Annu. Rev. Neurosci.* **28**, 403–450 (2005).
23. M. E. Zink, L. Zhen, J. R. McHaney, J. Klara, K. Yurasits, V. E. Cancel, O. Flemm, C. Mitchell, J. Datta, B. Chandresekaran, A. Parthasarathy, Increased listening effort and cochlear neural degeneration underlie speech-in-noise deficits in normal-hearing middle-aged adults. *eLife* **13**, RP102823 (2025).
24. J. A. Bigalke, J. R. Carter, Sympathetic neural control in humans with anxiety-related disorders. *Compr. Physiol.* **12**, 3085–3117 (2022).
25. M. Grassmann, E. Vlemincx, A. von Leupoldt, J. M. Mittelstädt, O. Van den Bergh, Respiratory changes in response to cognitive load: A systematic review. *Neural Plast.* **2016**, 8146809 (2016).
26. M. Javorka, F. El-Hamad, B. Czippelova, Z. Turianikova, J. Krohova, Z. Lazarova, M. Baumert, Role of respiration in the cardiovascular response to orthostatic and mental stress. *Am. J. Physiol. Regul. Integr. Comp. Physiol.* **314**, R761–R769 (2018).
27. R. Obrist, *Cardiovascular Psychophysiology: A Perspective* (Plenum Press, 1981).
28. A. Sherwood, K. G. Allen, Beta-adrenergic mechanisms in cardiovascular responses to stress. *Psychophysiology* **27**, 633–647 (1990).
29. M. Brennan, M. Palaniswami, P. Kamen, Do existing measures of Poincaré plot geometry reflect nonlinear features of heart rate variability? *IEEE Trans. Biomed. Eng.* **48**, 1342–1347 (2001).
30. F. Shaffer, J. P. Ginsberg, An overview of heart rate variability metrics and norms. *Front. Public Health* **5**, 258 (2017).
31. C. E. Deuter, L. K. Kuehl, T. D. Blumenthal, A. Schulz, M. S. Oitzl, H. Schachinger, Effects of cold pressor stress on the human startle response. *PLOS ONE* **7**, e49866 (2012).
32. H. Jang, K. Sel, E. Kim, S. Kim, X. Yang, S. Kang, K.-H. Ha, R. Wang, Y. Rao, R. Jafari, N. Lu, Graphene e-tattoos for unobstructive ambulatory electrodermal activity sensing on the palm enabled by heterogeneous serpentine ribbons. *Nat. Commun.* **13**, 6604 (2022).
33. A. L. McRae, M. E. Saladin, K. T. Brady, H. Upadhyaya, S. E. Back, M. A. Timmerman, Stress reactivity: Biological and subjective responses to the cold pressor and Trier Social stressors. *Hum. Psychopharmacol.* **21**, 377–385 (2006).
34. G. Kapur, L. Chen, Y. Xu, K. Cashen, J. Clark, X. Feng, S. F. Wu, Noninvasive determination of blood pressure by heart sound analysis compared with intra-arterial monitoring in critically ill children—A pilot study of a novel approach. *Pediatr. Crit. Care Med.* **20**, 809–816 (2019).
35. L. Mourot, M. Bouhaddi, J. Regnard, Effects of the cold pressor test on cardiac autonomic control in normal subjects. *Physiol. Res.* **58**, 83–91 (2009).
36. S. O. Elias, R. E. Ajayi, Effect of sympathetic autonomic stress from the cold pressor test on left ventricular function in young healthy adults. *Physiol. Rep.* **7**, e13985 (2019).
37. S. A. Sands, P. I. Terrill, B. A. Edwards, L. T. Montemurro, A. Azarbarzin, M. Marques, C. M. de Melo, S. H. Loring, J. P. Butler, D. P. White, A. Wellman, Quantifying the arousal threshold using polysomnography in obstructive sleep apnea. *Sleep* **41**, zsx183 (2018).
38. P. E. Brockmann, J. L. Perez, A. Moya, Feasibility of unattended home polysomnography in children with sleep-disordered breathing. *Int. J. Pediatr. Otorhinolaryngol.* **77**, 1960–1964 (2013).
39. P. Halász, M. Terzano, L. Parrino, R. Bódizs, The nature of arousal in sleep. *J. Sleep Res.* **13**, 1–23 (2004).
40. S. Kwon, H. S. Kim, S. H. Lee, W.-H. Yeo, Y.-T. Kwon, K. Kwon, H. Kim, J.-W. Jeong, Y. S. Kim, L. M. Trotti, A. Duarte, At-home wireless sleep monitoring patches for the clinical assessment of sleep quality and sleep apnea. *Sci. Adv.* **9**, eadg9671 (2023).
41. K. Seither, B. M. Helm, C. Heubi, D. Swarr, K. R. Suhrie, Sleep apnea in children with down syndrome. *Pediatrics* **151**, e2022058771 (2023).
42. J. de Miguel-Díez, J. R. Villa-Asensi, J. L. Álvarez-Sala, Prevalence of sleep-disordered breathing in children with Down syndrome: Polygraphic findings in 108 children. *Sleep* **26**, 1006–1009 (2003).
43. D. M. O'Driscoll, R. S. C. Horne, M. J. Davey, S. A. Hope, A. M. Walker, G. M. Nixon, The heart rate response to spontaneous arousal from sleep is reduced in children with Down syndrome referred for evaluation of sleep-disordered breathing. *Am. J. Physiol. Heart Circ. Physiol.* **298**, H1986–H1990 (2010).
44. M. B. Winn, D. Wendt, T. Koelewijn, S. E. Kuchinsky, Best practices and advice for using pupillometry to measure listening effort: An introduction for those who want to get started. *Trends Hear.* **22**, 2331216518800869 (2018).
45. J. R. McHaney, R. Tessmer, C. L. Roark, B. Chandrasekaran, Working memory relates to individual differences in speech category learning: Insights from computational modeling and pupillometry. *Brain Lang.* **222**, 105010 (2021).
46. A. P. Allen, P. J. Kennedy, S. Dockray, J. F. Cryan, T. G. Dinan, G. Clarke, The Trier Social Stress Test: Principles and practice. *Neurobiol Stress* **6**, 113–126 (2017).
47. K. S. Quigley, P. J. Gianaros, G. J. Norman, J. R. Jennings, G. G. Berntson, E. J. C. de Geus, Publication guidelines for human heart rate and heart rate variability studies in psychophysiology—Part 1: Physiological underpinnings and foundations of measurement. *Psychophysiology* **61**, e14604 (2024).

Acknowledgments

Funding: This work was supported by the Querrey-Simpson Institute for Bioelectronics at Northwestern University. S.H.K. acknowledges funding from a grant of the Korea Health Technology R&D Project through the Korea Health Industry Development Institute (KHIDI), funded by the Ministry of Health and Welfare, Republic of Korea (grant number: HI19C075300). S.H.K. acknowledges funding supported by the 2025 Advanced Facility Fund of the University of Seoul. T.W.P. acknowledges funding from the National Research Foundation of Korea (NRF) grant funded by the Korea government (MSIT) (no. RS-2023-00242507). Y.H.J. acknowledges funding from the National Research Foundation of Korea (NRF) grant NRF-2022R1C1C1003994 funded by the MSIT of the Korean government. J.-Y.Y. acknowledges funding from the Basic Research Laboratory (BRL) Project from National Research Foundation (RS-2024-00406674) funded by the Ministry of Science and ICT of Korea. **Author contributions:** S.H.K., T.W.P., S.C., T.Y., D.E.W.-M., J.-Y.Y., and J.A.R. conceived the idea, designed the research, and wrote the manuscript. S.H.K., T.W.P., T.Y., and J.-Y.Y. supervised the design and conceptualization of the device and carried out mold design based on software and device fabrication. J.-Y.Y. designed the graphical user interface. S.H.K., T.W.P., and S.C. developed and operated the protocols. S.H.K., T.Y., and J.-Y.Y. analyzed the clinical data. S.H.K., T.W.P., S.C., T.Y., D.E.W.-M., J.-Y.Y., and J.A.R. carried out experimental validation and analysis. Y. Wu, J.J., J.P., H.-Y.A., A.K., K.I., J.R.M., and M.-S.J. conducted investigation, contributed clinical resources, and supported data validation and visualization. S.Y., Y.Wa., J.-K.C., J.T., and S.O. contributed to methodology, software development, data curation, formal analysis, and validation. Y.H.J. and S.M.W. contributed to supervision, conceptualization, funding acquisition, and project administration. S.H.K., T.W.P., S.C., T.Y., S.Y., K.I., J.R.M., J.J., A.K., Y.Wa., Y. Wu, J.-K.C., J.P., H.-Y.A., M.-S.J., J.T., Y.H.J., S.O., S.M.W., D.E.W.-M., J.-Y.Y., and J.A.R. have all read, revised, and approved the final version of the manuscript. **Competing interests:** The authors declare that they have no competing interests. **Data, code, and materials availability:** All data and code needed to evaluate and reproduce the conclusions in the paper are present in the paper and/or the Supplementary Materials. Data presented in this study are not publicly available due to the protection of research participant privacy. Completely deidentified human subject data can be provided by the Research Director of the Querrey-Simpson Institute for Bioelectronics (QSIB; tbanks@northwestern.edu) pending scientific review and a completed data use agreement with Northwestern University and Ann & Robert H. Lurie Children's Hospital of Chicago.

Submitted 23 October 2025
Accepted 8 April 2026
Published 13 May 2026
10.1126/sciadv.aed3162

Science Advances

Wireless, skin-interfaced multimodal sensing system for continuous psychophysiological monitoring—A wearable polygraph device

Sun Hong Kim, Tae Wan Park, Seunghee Cho, Tianyu Yang, Seonggwang Yoo, Khaytin Ilya, Jacie R. McHaney, Jana Jaffe, Anisha Kshetrapal, Yue Wang, Yunyun Wu, Jan-Kai Chang, Jihun Park, Hak-Young Ahn, Min-Seung Jo, Jacob Trueb, Yei Hwan Jung, Seyong Oh, Sang Min Won, Debra E. Weese-Mayer, Jae-Young Yoo, and John A. Rogers

Sci. Adv. **12** (20), eaed3162. DOI: 10.1126/sciadv.aed3162

Science Advances (ISSN 2375-2548) is published by the American Association for the Advancement of Science. 1200 New York Avenue NW, Washington, DC 20005. The title *Science Advances* is a registered trademark of AAAS.